

## Systematic study of the stopping power of the lanthanides

J. P. Peralta <sup>\*</sup>, A. M. P. Mendez , D. M. Mitnik , and C. C. Montanari 

*Instituto de Astronomía y Física del Espacio, CONICET and Universidad de Buenos Aires, 1428 Buenos Aires, Argentina*

 (Received 21 December 2022; revised 17 February 2023; accepted 2 May 2023; published 23 May 2023)

In the last decade, lanthanides have become the subject of multiple studies due to their importance in technological applications. This paper aims to systematically study the energy loss per unit length of protons on the 15 lanthanides, from lanthanum to lutetium. We investigate the stopping power cross sections by considering the influence of the relativistic atomic structure, namely the description of the  $4f$  electrons, the number of electrons in the valence shells, and the electronic screening of the same or close subshells. The electronic stopping model considers separate contributions from bound and valence electrons. We employ a many-electron model for the former and a combination of perturbative and nonperturbative free-electron gas approaches for the latter. Our stopping results for the lanthanide series cover an extended energy range from very low to the MeV region. We compare them with measurements and other theoretical (DPASS, CASP) and semiempirical (SRIM) methods. Our results agree with most experimental data, even the recent values around the maximum for gadolinium. We implement Lindhard's scaling for the stopping number for all the data available of the 15 targets. Lindhard scaling for the stopping number includes all the data for the 15 targets. The present paper casts doubts on certain data sets, which should affect SRIM's description of lanthanides, such as La, Nd, Dy, and Tb. We call attention to the scarcity of measurements in the low and intermediate ranges, and we suggest experimental efforts to shed light on the stopping power of these relevant targets.

DOI: [10.1103/PhysRevA.107.052809](https://doi.org/10.1103/PhysRevA.107.052809)

### I. INTRODUCTION

Lanthanides, also known as rare-earth elements (REEs), encompass 15 atoms: lanthanum, cerium, praseodymium, neodymium, promethium, samarium, europium, gadolinium, terbium, dysprosium, holmium, erbium, thulium, ytterbium, and lutetium. These elements feature nuclear charges ranging from 57 to 71 and have interesting properties, mainly related to the filling of the  $4f$  subshell. Recent studies on REEs and their alloys are driven by their practical applications, such as high-tech devices, computer information storage, energy-saving gadgets (green technology), superconductors, and medicine [1–3]. For example, lutetium has essential medical applications in cancer therapy [4]. On a side note, promethium is the only one that is radioactive, being the product of nuclear reactions (spontaneous fission of uranium and alpha decay of  $^{151}\text{Eu}$ ).

The energy loss or stopping power of lanthanides is still an open subject. Regarding the theoretical description of the atomic structure, solving such multielectronic targets poses a real challenge. As demonstrated in previous works [5–8], fully relativistic calculations are required for the inner electrons, which also affect the description of the outer shells, such as the  $4f$ . Moreover, we showed in Ref. [5] that stopping calculations based on nonrelativistic atomic structure underestimate the values around the maximum.

On the experimental side, the stopping data of hydrogen in some lanthanides (Ce, Pr, Sm, Ho, Er, Yb) are very scarce (few data points in a narrow energy region). Moreover, in

other cases (Pm, Eu, Tm), the data are nonexistent. In the case of Nd, Tb, Dy, and Lu, the only experimental data are the measurements by Krist and Mertens [9,10] from 1983. However, in the same publications, the stopping data for other targets (Al, Au, Ag, Ta, Pt) have been shown to disagree with most experimental values [11]. The case of Gd is exceptional; there are multiple data sets in an extended energy range. Recent measurements [12] for this target differ from previous data [13] and the SRIM predictions [14] at impact energies around the stopping maximum and below.

In compounds, most lanthanides bond with valence +3, but also +2 and +4 [2,15]. When dealing with metallic lanthanides, the question is whether this configuration remains in the solid phase and how many electrons per atom are part of the metallic conduction band.

This paper aims to study the stopping power of REEs for protons systematically. We pay special attention to the influence of the atomic structure on the cross sections, including the number of valence electrons, the promotion of  $4f$  electrons in the conduction band, and the screening among electrons of the same or even close subshells. To this end, we employed a free-electron gas (FEG) description for the valence electrons and the shellwise local plasma approximation (SLPA) [16] for the bound shells. The combination of these formalisms proved to properly describe the energy loss in metals in an extended energy range [17]. Moreover, the very good agreement with recent experimental data for postlanthanides, Ta and Pt, encouraged us to extend the study to the lanthanide series [6]. The whole picture given by this systematic study not only helps improve the theoretical description but also casts doubts on some experimental data sets.

\*jpperalta@iafe.uba.ar

The paper is organized as follows: we present the atomic structure approach in Sec. II and the stopping power models employed in Sec. III. Theoretical results and comparisons with the experimental data are included and discussed in Sec. IV. Finally, Sec. V summarizes the conclusions of the present paper. Atomic units are employed, except where otherwise mentioned.

## II. ATOMIC STRUCTURE MODEL

The single-particle Dirac equation for a potential  $V(\mathbf{r})$  is

$$h^D \varphi_{nljm}(\mathbf{r}) = E_{nlj} \varphi_{nljm}(\mathbf{r}), \quad (1)$$

where  $h^D = T^D + V$  is the single-electron Dirac Hamiltonian, and  $T^D$  is the single-particle kinetic operator. In atomic units, this operator is given by

$$T^D = c \boldsymbol{\alpha} \cdot \mathbf{p} + \beta c^2. \quad (2)$$

The constant  $c$  is the speed of light, and the quantities  $\boldsymbol{\alpha}$  and  $\beta$  are  $4 \times 4$  Dirac matrices

$$\boldsymbol{\alpha} = \begin{pmatrix} 0 & \boldsymbol{\sigma} \\ \boldsymbol{\sigma} & 0 \end{pmatrix}, \quad \beta = \begin{pmatrix} \mathbf{I} & 0 \\ 0 & -\mathbf{I} \end{pmatrix}, \quad (3)$$

the  $2 \times 2$  matrix  $\boldsymbol{\sigma}$  is the Pauli spin matrix,  $\mathbf{I}$  is the unitary matrix of rank 2, and  $\mathbf{p} = -i\nabla$ . The atomic fully relativistic states are obtained from the many-electron Dirac Hamiltonian:

$$\mathbf{H}^D = \sum_i \left[ T_i^D - \frac{Z}{r_i} \right] + \sum_{i < j} \frac{1}{r_{ij}}, \quad (4)$$

where the last terms are the nuclei-electron and the electron-electron interactions.

In our paper, we solved the fully relativistic atomic structure using the HULLAC code package (for more details, see Ref. [18] and references therein). In particular, from this suite, the RELAC code was used to calculate first-order energies and wave functions, implementing the relativistic parameter potential. In this approach, the Dirac Hamiltonian is split into a zeroth-order part and a perturbation:

$$\mathbf{H}^D = \mathbf{H}_0 + \mathbf{H}_1. \quad (5)$$

The zeroth-order Hamiltonian contains a spherical potential  $U(r)$  representing the screening of the charge distribution (averaging the interaction between the electrons), and is written as

$$\mathbf{H}_0 = \sum_i [T_i^D + U(r_i)]. \quad (6)$$

The perturbation is

$$\mathbf{H}_1 = \sum_i \left[ -\frac{Z}{r_i} - U(r_i) \right] + \sum_{i < j} \frac{1}{r_{ij}}. \quad (7)$$

The key component of the parameter potential method resides in the election of the spherical  $U(r)$  in such a way that the perturbation  $\mathbf{H}_1$  becomes small, minimizing the first-order configuration averaged energies. The specific form of the potential and the procedure for obtaining the solutions of the many-electron states is discussed in Ref. [18].

The parametric potential method is implemented within the configuration-interaction (CI) scheme, i.e., the potential is minimized for different groups of configurations clustered by similar energies and the same parity. The Hamiltonian  $\mathbf{H}^D$  is then constructed based on the mixed configurations included in the  $U(r_i)$  calculation, allowing us to take into account correlation effects.

Since we are dealing with a central potential, it is possible to separate the radial and angular coordinates, expressing the solutions as spinors:

$$\varphi_{nljm}(\mathbf{r}) = \frac{1}{r} \begin{pmatrix} i P_{nlj}(r) \Omega_{ljm}(\hat{r}) \\ Q_{nlj}(r) \Omega_{-ljm}(\hat{r}) \end{pmatrix}, \quad (8)$$

where  $P_{nlj}(r)$  and  $Q_{nlj}(r)$  are the radial large and small spinor components, respectively, and  $\Omega$  are spherical spinors. The normalization conditions for the orbitals

$$\int \varphi_{nljm}^\dagger(\mathbf{r}) \varphi_{nljm}(\mathbf{r}) d\mathbf{r} = 1 \quad (9)$$

can be written as

$$\int_0^\infty [P_{nlj}^2(r) + Q_{nlj}^2(r)] dr = 1. \quad (10)$$

Similarly, the mean radius can be obtained by

$$\langle r \rangle_{nlj} = \int_0^\infty [P_{nlj}^*(r) r P_{nlj}(r) + Q_{nlj}^*(r) r Q_{nlj}(r)] dr. \quad (11)$$

For the relativistic orbitals, we use the notation  $nl\pm$ , which means  $nlj$ , where the index  $j = l \pm 1/2$  is referred to as  $\pm$ . The  $N$ -electron zeroth-order solutions are constructed from antisymmetrized products of orbitals.

Following Grant [19], the Breit interaction and QED corrections are treated as second perturbations. The total Hamiltonian is given by

$$\mathbf{H} = \mathbf{H}^D + \mathbf{H}_{\text{Breit}} + \mathbf{H}_{\text{QED}}, \quad (12)$$

where the Breit interaction

$$\mathbf{H}_{\text{Breit}} = \sum_{i < j} -\boldsymbol{\alpha}_i \cdot \boldsymbol{\alpha}_j \frac{\cos(\omega r_{ij})}{r_{ij}} + (\boldsymbol{\alpha}_i \cdot \nabla_i)(\boldsymbol{\alpha}_j \cdot \nabla_j) \frac{\cos(\omega r_{ij}) - 1}{\omega^2 r_{ij}} \quad (13)$$

is produced by the emission of a virtual photon of energy  $\omega$  from electron  $i$  and its capture by another electron  $j$ . The  $\mathbf{H}_{\text{QED}}$  represents the additional quantum electrodynamic corrections given by the vacuum polarization and the self-energy.

Selecting the correct configurations included in the CI is vital for the electron structure calculation of elements. In general, configurations with the same parity are included. Then, their respective energy levels mix, and important correlation effects are accounted for. However, the lanthanides feature an open  $4f$  subshell, which may lead to electronic structures of hundreds of levels when including just one configuration. A careful selection of mixing configurations is considered in this paper, which is further discussed in Sec. IV A.

### III. THE ENERGY-LOSS MODELS

#### A. Stopping power of valence electrons

At low-impact energies, the electronic stopping power is governed by the interaction of the projectile with the valence electrons. In metals, the representation of the conduction electrons as a FEG has been proven successful [20–22]. This FEG is characterized by its density, which is usually expressed in terms of the Wigner-Seitz radii per electron,  $r_s$ .

Following previous works [6,17,23], we use two models to describe the stopping for a projectile moving in a FEG: (i) the screened potential with cusp condition (SPCC) model [17], which is a nonlinear binary collisional approach, and (ii) the Mermin-Lindhard dielectric formalism [24], which is a linear-response approximation that includes binary and collective excitations (plasmons). Consequently, we can model the FEG contribution in an extensive energy range by using the SPCC model at low to intermediate energies and the Mermin-Lindhard formalism at intermediate- to high-energy values, where plasmon excitations are important.

#### B. Stopping power of bound electrons

The energy loss due to the ionization of the bound electrons is described using the SLPA [16]. This collective description allows including electrons from the  $4f$  orbital down to the  $K$  shell with the same level of complexity. This model has been successfully used to describe the different moments of the energy loss, i.e., stopping [6,23], straggling [25], and ionization of different shells [26–28]. Noteworthy, the SLPA verifies the  $f$ -sum rules and Bethe high-energy limit [6,16].

The stopping power for a bare ion with charge  $Z_p$ , moving at velocity  $v$ , in the SLPA is obtained by adding the independent  $nl$  contributions defined as

$$S_{nl} = \frac{2}{\pi v^2} \int_0^\infty \frac{Z_p^2 dk}{k} \int_0^{kv} \omega \operatorname{Im} \left[ \frac{-1}{\varepsilon_{nl}(k, \omega)} \right] d\omega. \quad (14)$$

The imaginary part of the inverse dielectric function is expressed as

$$\operatorname{Im} \left[ \frac{-1}{\varepsilon_{nl}(k, \omega)} \right] = \rho_a \int \operatorname{Im} \left[ \frac{-1}{\varepsilon^{\text{SLPA}}(k, \omega, \rho_{nl}(r))} \right] d\mathbf{r}, \quad (15)$$

with  $\rho_a$  being the target atomic density and  $\rho_{nl}(r)$  being the local density of electrons of the  $nl$  subshell. Note that a local density implies a local plasmon frequency  $\omega_p^{nl}(r) = \sqrt{4\pi \rho_{nl}(r)}$ . Following Ref. [6], the dielectric function  $\varepsilon^{\text{SLPA}}$  employed in Eq. (15) is that of Levine-Mermin (LM), which allows including explicitly the energy gap of each subshell and a local damping  $\gamma_p^{nl}(r) = \omega_p^{nl}(r)/2$ . We call this proposal SLPA-LM. It is essential to highlight that the only inputs of the SLPA-LM model are the electronic structure solutions described in Sec. II, i.e., orbital radial densities  $\rho_{nl\pm}(r)$  and binding energies  $E_{nl\pm}$ .

The relativistic binding energies present spin-orbit splits. However, Heisenberg's uncertainty,  $\Delta E \Delta t \geq \hbar/2$ , makes this split vanish for very short collisional times. We roughly estimate  $\Delta t \approx 2\langle r \rangle_{nl}/v$ , with  $\langle r \rangle_{nl}$  and  $v$  being the mean orbital radii and the ion velocity, respectively. Using this criterion, the SLPA describes the  $nl\pm$  electrons together as a single electronic density  $\rho_{nl}(r)$  with mean binding energy  $E_{nl}$ . The

physical consequence of this approach is ensuring intrashell screening among these electrons [7,8].

Analogously, above certain impact velocities, we consider intershell screening among electrons belonging to different orbitals but with very close binding energies. We successfully implemented this criterion to the  $5p$  and  $4f$  electrons of heavy transition metals (Hf, Ta, W, and Pt) [5,6]. The case of the REE is somewhat different because, although the  $4f$  electrons are localized close to the  $5p$  orbital, they are loosely bound. We estimate a threshold velocity  $v_{pf} \approx \Delta E_{pf} 2\langle r \rangle_{pf}/(\hbar/2)$ , where  $\Delta E_{pf} = |E_{4f} - E_{5p}|$  is the energy gap between the  $4f$  and  $5p$  subshell, and  $\langle r \rangle_{pf}$  is the mean  $r$  value of the combined electron density of these shells. For impact velocities  $v > v_{pf}$ , we consider these electrons to respond to the incoming projectile as a single electronic cloud.

### IV. RESULTS AND DISCUSSION

This section presents our full theoretical results of atomic structure and electronic stopping power for protons on all the elements from the lanthanide series. The present stopping power calculations consider separate inner (bound) and outer (valence) electronic contributions to the energy loss. Hence, the proper bound-valence separation is crucial. We present the results as follows: first, the atomic structure calculations to describe the inner bound electrons; secondly, the discussion about the valence electrons; and finally, the total stopping power results.

#### A. Atomic structure calculations

The ground-state configuration of atomic lanthanides can be generally expressed as  $[\text{Xe}] 4f^{n+1} 6s^2$  or  $[\text{Xe}] 4f^n 5d 6s^2$ . According to the  $n$  number of electrons in the  $4f$  subshell, lanthanides can be light (La to Eu) or heavy (Gd to Lu).

As described in Sec. II, the atomic structure was computed by introducing a CI scheme, which considers the ground configuration and contributing excited states. We present these ground configurations in Table I. The excited states included in the CI were selected by considering the parity of the promoted electrons and the closeness of the energy levels of said excited electrons. For example, we included two electronic configurations for Ce: the ground  $4f 5d 6s^2$  and the excited  $4f 5d^3$  states. Details about the CI included in the calculation for Gd and Er can be found in Ref. [29]. A similar approach was followed for the computation of the remaining atomic systems.

The present binding energy results are shown in Figs. 1–6 with filled symbols. These values for atoms can be compared to those in solid targets up to the subvalence shell. The outer electrons in a solid are considered part of the FEG, as will be discussed later in Sec. IV B.

The results for La are presented in Fig. 1, which is the first in the lanthanide series and has no  $4f$  electrons. Figure 2 illustrates the values for Ce, Gd, and Lu. We grouped these elements since they are the only REE with  $5d$  electrons. Another characteristic to bear in mind about this arrangement is that Ce has one electron in the  $4f$  subshell, while Gd and Lu feature a half-filled and completely filled subshell, respectively. The binding energies for the rest of the lanthanides are

TABLE I. Atomic structure and valence electrons data from La to Lu:  $Z$ , nuclear charge; electronic configuration;  $E_{4f\pm}^{\text{exp}}$ , experimental measurements (mean value) of the  $4f$  subshell;  $E_{4f}$  and  $\langle r \rangle_{4f}$ , present theoretical calculations for binding energy and mean radii of the  $4f$  subshell;  $N_e$ , the number of valence electrons per atom;  $r_s$ , the Wigner-Seitz radii;  $\omega_p$ , the plasmon frequency,  $\gamma_p$ , the half width of the plasmon peak;  $E_F$ , the Fermi energy; and  $E_p$ , the minimum proton energy to excite plasmons.

	$Z$	Electronic configuration	$E_{4f\pm}^{\text{exp}}$ (eV)	$E_{4f}$ (eV)	$\langle r \rangle_{4f}$ (a.u.)	$N_e$	$r_s$ (a.u.)	$\omega_p$ (a.u.)	$\gamma_p^{\text{exp}}$ (a.u.)	$E_F$ (a.u.)	$E_p$ (keV)
La	57	[Xe] 5d 6s <sup>2</sup>				3	2.72	0.386	0.15	0.25	24
Ce	58	[Xe] 4f 5d 6s <sup>2</sup>	0.1 ± 1.2	5.2	1.098	4	2.40	0.466	0.15	0.32	30
Pr	59	[Xe] 4f <sup>3</sup> 6s <sup>2</sup>	2.0 ± 0.6	2.6	1.176	3	2.66	0.398	0.15	0.26	25
Nd	60	[Xe] 4f <sup>4</sup> 6s <sup>2</sup>	1.5 ± 0.9	2.2	1.125	3	2.64	0.404	0.15	0.26	25
Pm	61	[Xe] 4f <sup>5</sup> 6s <sup>2</sup>		8.8	1.060	3	2.61	0.410	0.15	0.27	26
Sm	62	[Xe] 4f <sup>6</sup> 6s <sup>2</sup>	5.5 ± 1.1	11.4	0.925	3	2.61	0.410	0.15	0.27	26
Eu	63	[Xe] 4f <sup>7</sup> 6s <sup>2</sup>	0.0 ± 3.2	1.8	1.140	3	2.96	0.341	0.15	0.21	21
Gd	64	[Xe] 4f <sup>7</sup> 5d 6s <sup>2</sup>	8.3 ± 0.1 <sup>c</sup>	10.7	0.926	3	2.61	0.411	0.15	0.27	26
Tb	65	[Xe] 4f <sup>9</sup> 6s <sup>2</sup>	2.6 ± 1.5	3.4	0.995	2	2.96	0.341	0.15	0.21	21
Dy	66	[Xe] 4f <sup>10</sup> 6s <sup>2</sup>	4.2 ± 1.6	5.0	0.870	2	2.94	0.344	0.15	0.21	21
Ho	67	[Xe] 4f <sup>11</sup> 6s <sup>2</sup>	3.7 ± 3.0	4.8	0.852	2	2.93	0.346	0.15	0.21	21
Er	68	[Xe] 4f <sup>12</sup> 6s <sup>2</sup>	4.3 ± 1.4	4.2	0.828	2	2.91	0.349	0.15	0.22	21
Tm	69	[Xe] 4f <sup>13</sup> 6s <sup>2</sup>	5.3 ± 1.9	2.9	0.825	2	2.89	0.352	0.15	0.22	22
Yb	70	[Xe] 4f <sup>14</sup> 6s <sup>2</sup>	6.3 ± 1.0	3.0	0.787	2	3.22	0.300	0.15	0.18	18
Lu	71	[Xe] 4f <sup>14</sup> 5d 6s <sup>2</sup>	6.9 ± 0.5	10.6	0.723	3	2.51	0.435	0.15	0.29	27

<sup>a</sup>Values extracted from Ref. [31] except for Gd.

<sup>b</sup>Taken from Ref. [35] for Tb and applied to all the REE.

<sup>c</sup>Taken from Ref. [34].

displayed in Figs. 3 (Nd, Pm, and Sm), 4 (Pr, Eu, and Tb), 5 (Dy, Ho, and Er), and 6 (Tm and Yb). The energy values for some targets were multiplied by a factor of 10 or 100 to contrast overlapping results. We compared the present theoretical calculations with the solid-state experimental measurements compiled by Williams [30], which include data from Ref. [31].

Our calculations agree excellently with the experimental values for the deepest electrons, i.e.,  $K$  ( $< 1\%$ ),  $L$  ( $< 2\%$ ), and  $M$  ( $< 4\%$ ) shells. For the  $N$  shell, our results are still good ( $< 7\%$ ), except for  $4d$  electrons in Eu, Sm, and Pm ( $\approx 10\%$ ). The subvalence shells are the orbitals with the most differences and will be discussed below.

For the  $5s$  and  $5p$  orbitals, we find differences of up to 10% except for La, Ce, Tb, Dy, and Lu, which are less than

25%. Generally, these values rise due to the contrasting nature of the experimental measurements (solid) versus our atomic calculations, which may be considered gaseous. Larger discrepancies in these subvalence orbitals are found for Gd and Eu, of approximately 75% (Figs. 2 and 4). These differences do not originate in the solid-atomic dissimilarities but are a theoretical shortcoming due to the large number of quantum states belonging to the partially filled  $f^7$  subshell. For Pm, there are no experimental values for the subvalence orbitals  $5s$ ,  $5p$ , and  $4f$ . Data for Pm are generally scarce, which may be related to its radioactive nature.

Given the importance of the  $4f$  subshell in lanthanides, we included in Table I the present mean radii  $\langle r \rangle_{4f}$ , the binding energy  $E_{4f}$ , and its corresponding experimental measurement

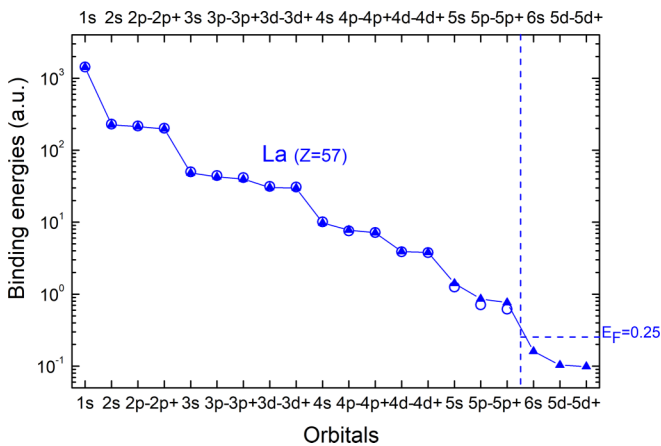


FIG. 1. Electron binding energies of La. Present relativistic calculation ( $\blacktriangle$  symbols) and experimental values from Ref. [30] ( $\circ$  symbols).

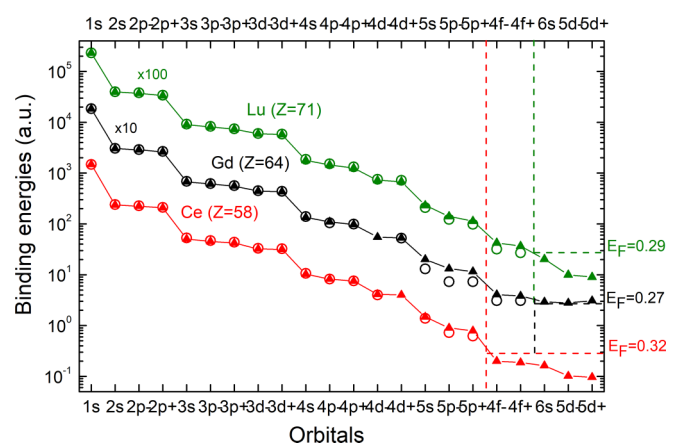


FIG. 2. Electron binding energies of Ce, Gd, and Lu. Present relativistic calculation ( $\blacktriangle$  symbols) and experimental values from Ref. [30] ( $\circ$  symbols).

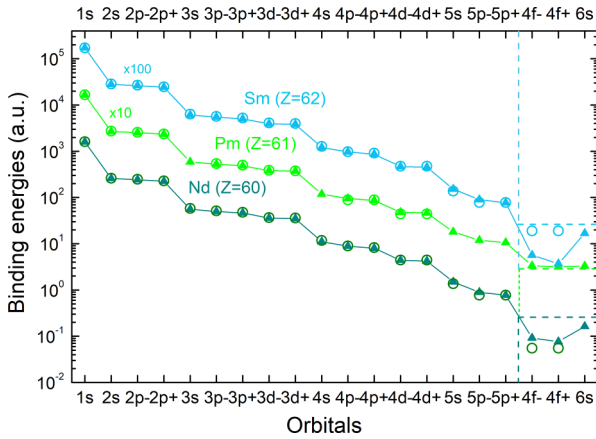


FIG. 3. Electron binding energies of Nd, Pm, and Sm. Present relativistic calculation ( $\blacktriangle$  symbols) and experimental values from Ref. [30] ( $\circ$  symbols).

$E_{4f}^{\text{exp}}$  (and error). As the nuclear charge increases and the 4*f* orbital fills, we observe the well-known lanthanide radii contraction. This effect is mainly responsible for most of its spectroscopic and magnetic properties [32]. The binding energies of 4*f* electrons have been shown to change according to the metal's valence configuration [33]. So, the discrepancies found may be related to the gas-solid differences mentioned above. On a side note, the experimental 4*f*± binding energy of Eu is  $E_{4f\pm} = 0 \pm 3.2$  eV [31]. This value is not included in Fig. 4, but the mean value of the corresponding theoretical prediction is contained within the experimental error, as shown in Table I.

**B. Lanthanide valence electrons**

As previously described, the present stopping power calculations are based on the separate inner and valence shell (or FEG) contributions to the energy loss. Although the results displayed in Figs. 1–6 are for gas atoms, we included a vertical dashed line that illustrates the gas-solid difference; i.e., from the vertical line to the right, the electrons belong to the FEG

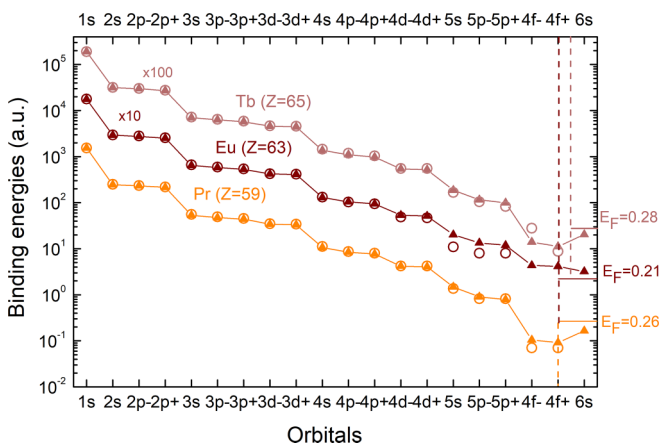


FIG. 4. Electron binding energies of Pr, Eu, and Tb. Present relativistic calculation ( $\blacktriangle$  symbols) and experimental values from Ref. [30] ( $\circ$  symbols).

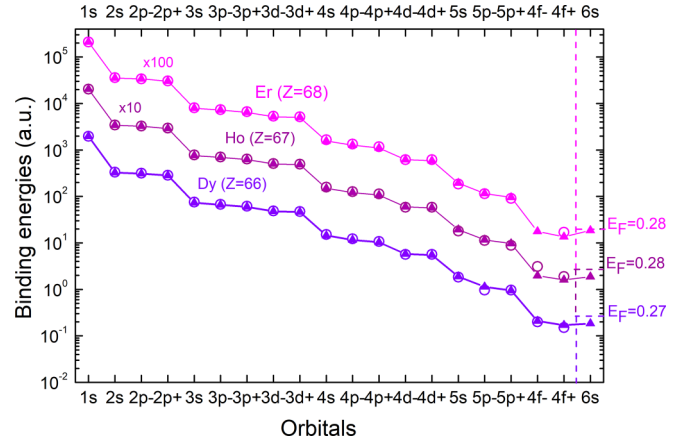


FIG. 5. Electron binding energies of Dy, Ho, and Er. Present relativistic calculation ( $\blacktriangle$  symbols) and experimental values from Ref. [30] ( $\circ$  symbols).

and the bound states in this region are not valid. The horizontal dashed lines indicate the corresponding Fermi energy,  $E_F$ .

For most elements in the periodic table, a straightforward comparison between atomic binding energies and experimental measurements in solids would suggest the bound-valence separation. Generally, valence shells with no experimental measurements may indicate that their corresponding electrons belong to the conduction band.

As shown in Fig. 1 for La, there are no experimental values for the 5*d* and 6*s*<sup>2</sup> orbitals; hence, it is reasonable to consider the number of electrons in the FEG:  $N_e = 3$ . We can also note that the band gap ( $0 < E < E_F$ ) encompasses the atomic 5*d* and 6*s* electrons. Moreover, the energy gap between the 5*p* electrons and the valence shells unequivocally supports our suggestion.

For the other elements in the lanthanide series, the discussion of the bound-valence separation is analogous to the case of La, with a few exceptions. For Ce (Fig. 2), we propose  $N_e = 4$  electrons in the FEG, which correspond to the 4*f* 5*d* 6*s*<sup>2</sup> configuration. Metallic cerium has been reported to show spontaneous interconfiguration fluctuations between +3

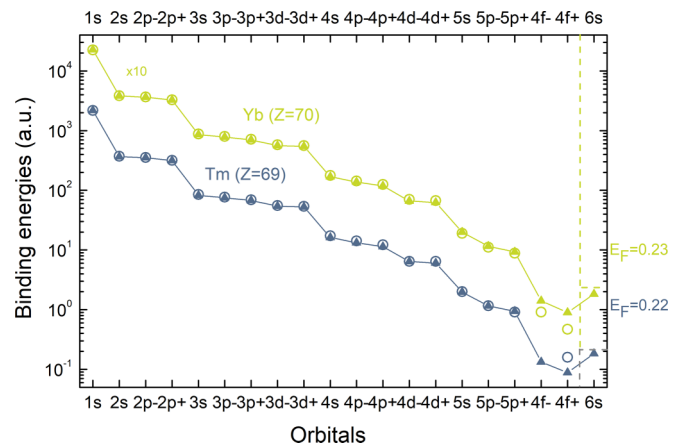


FIG. 6. Electron binding energies of Tm and Yb. Present relativistic calculation ( $\blacktriangle$  symbols) and experimental values from Ref. [30] ( $\circ$  symbols).

and +4. The itinerant nature of the  $4f$  electron in metals has been related to its chemical environment or pressure [36]. The  $4f$  electron promoted to the FEG is also suggested for the rest of the light lanthanides: Pr, Nd, Pm, Sm, and Eu (Figs. 3 and 4) [33,36,37]. Thus, we considered for these targets  $N_e = 3$ , i.e., one  $4f$  and two  $6s$  electrons.

The case of Gd and Lu (Fig. 2) is different; their electronic configuration includes one  $5d$  electron (see Table I). We found that the  $4f$  electrons are strongly correlated, which leads us to consider  $N_e = 3$ , i.e.,  $5d 6s^2$  valence electrons in the conduction band and all  $4f$  electrons in the bound shells. Similarly, for the rest of the heavy lanthanides (Tb, Dy, Ho, Er, Tm, and Yb), shown in Figs. 4–6, we suggest  $N_e = 2$ , i.e., two electrons from the  $6s$  subshell in the FEG. Although the  $4f$  electrons of these elements are still loosely bound, the mean radii are smaller than 1 a.u., as can be seen in Table I. Our proposal agrees with other *ab initio* studies, which conclude that these metallic elements feature +2 electrons in their valence configuration [37].

In summary, the present systematic analysis performed led us to consider one  $4f$  electron in the FEG for the light lanthanides ( $Z = 58$ –63) and none for the rest. The number of electrons in the FEG inferred for the 15 REEs is presented in Table I. We also include the corresponding FEG parameters in Table I: the Wigner-Seitz radii  $r_S$ , the plasmon frequency  $\omega_p$ , and  $E_F$ , which are computed from the value of  $N_e$ .

### C. Stopping power calculations

The density of electrons in the FEG is the most critical parameter for describing the stopping power in the low-energy region. Both models employed here, SPCC and Mermin-Lindhard, depend on the density or equivalent parameter,  $r_S$  or  $\omega_p$ . The Mermin-Lindhard dielectric function relies on the  $\omega_p$  and  $\gamma_p$  values, with the latter being a finite value introduced by Mermin [24] as the probability of collisions per unit of time. When the momentum transferred tends to zero, this dielectric function approaches a Lorentzian function centered on  $\omega_p$  with half width at half maximum  $\gamma_p$ , experimentally observed in the optical energy-loss functions (ELFs).

The theoretical plasmon frequencies  $\omega_p$  presented in Table I were calculated using the proposed  $N_e$  values. Experimental ELF data for lanthanides are very scarce and dispersed [35,38]. Particularly, our computed  $\omega_p$  values are around 10 to 30% smaller than the experimental values reported by Colliex *et al.* [35] (except for Sm that is only 5% smaller); in general, they agree very well with the calculated ELF peaks obtained using the density-functional method [37].

Some studies [35,38] tabulate the experimental plasmon energy  $\omega_p$  and not the whole shape of the ELF, which is a predicament because knowing the energy-loss function allows one to obtain the width of the peak and the value of  $\gamma_p$ . The only exception we found in the literature is Tb [35] with  $\gamma_p(\text{Tb}) \simeq 0.15$  a.u. In the present calculations, we used this value for the 15 REEs. We investigated the dependence of the maximum stopping with the value of  $\gamma_p$ , which was found to be small ( $\lesssim 5\%$ ).

Another parameter we considered is the minimum energy for plasmon excitation,  $E_p$ . These values can be approached following the work from Ref. [39], and they are included

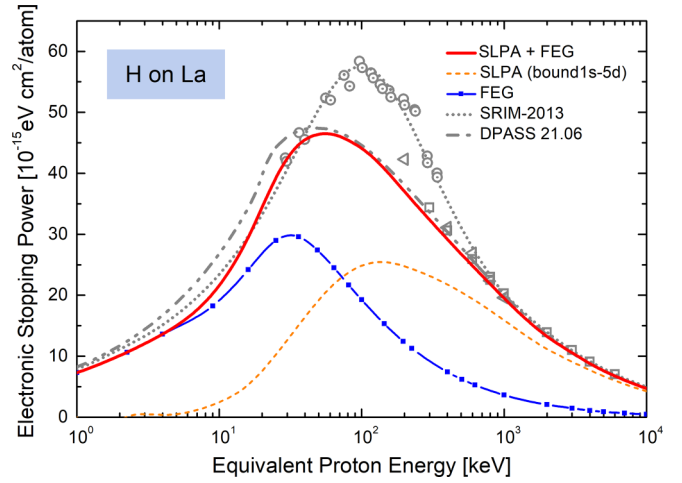


FIG. 7. Stopping cross section of La for H. Solid curves: present results using SLPA-LM—total (red solid line), bound electrons (1s–4f) (orange short-dashed line), and FEG values with  $r_S = 2.72$  ( $N_e = 3$ ) (blue squares-line). Discontinued curves: SRIM [14] (gray dotted line) and DPASS21.06 [45] (gray dash-double-dotted line). Symbols: experimental data from  $\diamond$  [46],  $\circ$  [9],  $\triangle$  [10], and  $\triangleleft$  [13].

in Table I for all the REEs. We employ the nonperturbative SPCC model, which does not include collective excitations, for energies below  $E_p$ , while for impact energies above  $E_p$  we use the Mermin-Lindhard model.

In Figs. 7–21, we display our theoretical electronic stopping power of REE for protons. It is worth mentioning that we are considering hydrogen in metals as protons; no neutral H or charge state effects are considered. The screening of the hydrogen nucleus by the free-electron gas makes the bound state of an electron to a proton very unlikely [39–41].

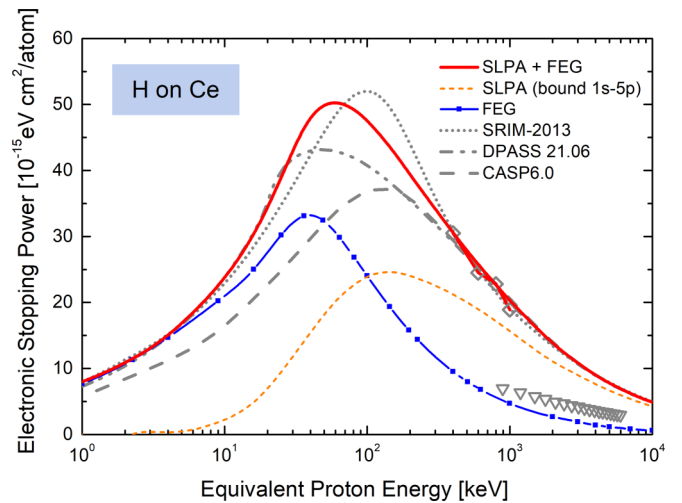


FIG. 8. Stopping cross section of Ce for H. Solid curves: present results using SLPA-LM—total (red solid line), bound electrons (1s–5p) (orange short-dashed line), and FEG with  $r_S = 2.40$  ( $N_e = 4$ ) (blue squares-line). Discontinued curves: SRIM [14] (gray-dotted line), DPASS21.06 [45] (gray-dash-double-dotted line), and CASP6.0 with  $r_S = 2.41$  ( $N_e = 4$ ) [42] (gray-dashed curve). Symbols: experimental data from  $\diamond$  [46] and  $\nabla$  [47].

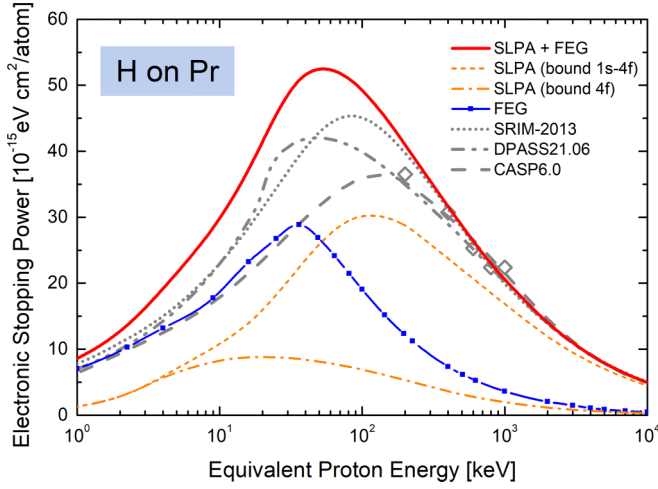


FIG. 9. Stopping cross section of Pr for H. Solid curves: present results using SLPA-LM—total (red solid line), bound electrons (1s-4f) (orange short-dashed line), and FEG with  $r_S = 2.66$  ( $N_e = 3$ ) (blue squares-line). Bound electrons (4f) (orange dash-dotted line). Discontinued curves: same as in Fig. 8, with  $r_S = 2.23$  ( $N_e = 5$ ) in CASP6.0. Symbols: experimental data from  $\diamond$  [46].

Three solid curves are included in each figure: the contribution of the FEG (blue line with squares), of the bound electrons (orange short-dashed curve), and the total stopping (red solid curve) resulting from adding the former two. We compare the present results with the available experimental data [11] and SRIM [14] predictions. In all the cases, we include the 4f and 5p intershell screening above the corresponding impact velocity  $v_{pf}$ , detailed in Sec. III B. We also include the results of two theoretical models: the convolution approximation for swift particles CASP version 6.0 by Schiwietz and Grande [42,43] and the binary theory of

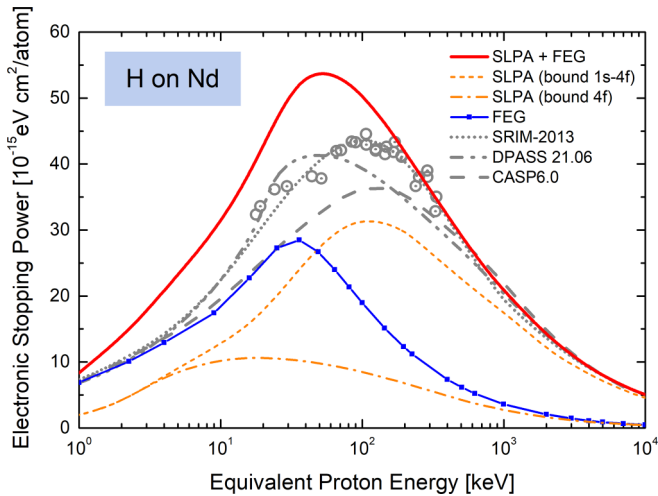


FIG. 10. Stopping cross section of Nd for H. Solid curves: present results using SLPA-LM—total (red solid line), bound electrons (1s-4f) (orange short-dashed line), and FEG with  $r_S = 2.64$  ( $N_e = 3$ ) (blue squares-line). Bound electrons (4f) (orange dash-dotted line). Discontinued curves: same as in Fig. 8, with  $r_S = 2.09$  ( $N_e = 6$ ) in CASP6.0. Symbols: experimental data from  $\circ$  [9] and  $\triangle$  [10].

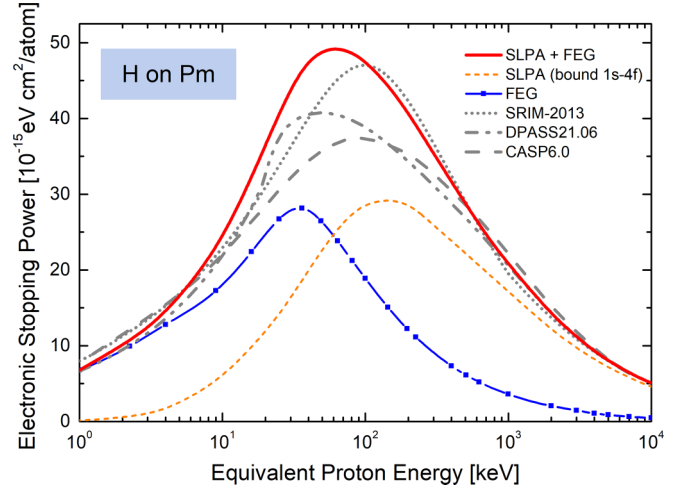


FIG. 11. Stopping cross section of Pm for H. Solid curves: present results using SLPA-LM—total (red solid line), bound electrons (1s-4f) (orange short-dashed line), and FEG with  $r_S = 2.61$  ( $N_e = 3$ ) (blue squares-line). Discontinued curves: same as in Fig. 8, with  $r_S = 2.05$  ( $N_e = 7$ ) in CASP6.0. No experimental data available.

electronic stopping by Schinner and Sigmund [44], included in the DPASS code version 21.06 [45]. Both models deal with the valence electrons as a FEG, while the inner shells are described using binary collisional approaches. In contrast to the perturbative models, DPASS and CASP include Barkas corrections and charge effects, and they can be applied to any ion-target combination in a wide energy range.

### 1. Lanthanum

In Fig. 7, we show the electronic stopping power of La for protons. For this target, the plasmon excitation threshold is  $E_p = 24$  eV, which separates the ranges of validity of the SPCC and the Mermin-Lindhard models for the FEG. The

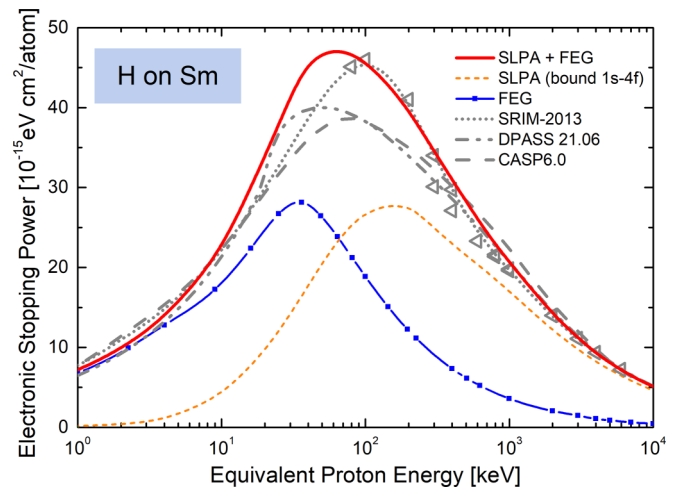


FIG. 12. Stopping cross section of Sm for H. Solid curves: present results using SLPA-LM—total (red solid line), bound electrons (1s-4f) (orange short-dashed line), and FEG with  $r_S = 2.61$  ( $N_e = 3$ ) (blue squares-line). Discontinued curves: same as in Fig. 8, with  $r_S = 1.88$  ( $N_e = 8$ ) in CASP6.0. Symbols: experimental data from  $\triangle$  [13].

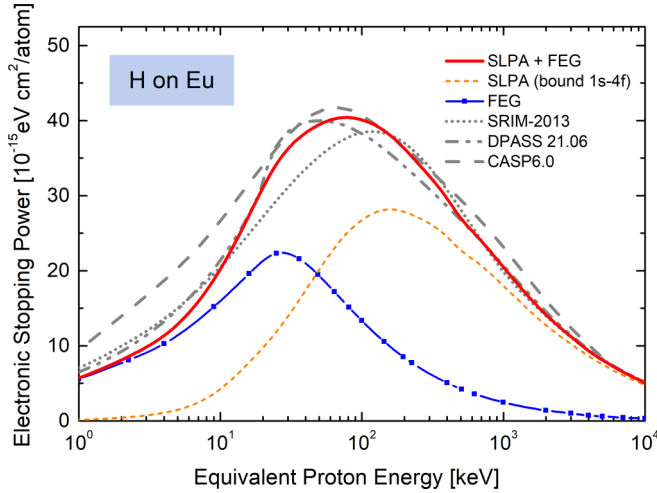


FIG. 13. Stopping cross section of Eu for H. Solid curves: present results using SLPA-LM—total (red solid line), bound electrons ( $1s-4f$ ) (orange short-dashed line), and FEG with  $r_S = 2.96$  ( $N_e = 3$ ) (blue squares-line). Discontinued curves: same as in Fig. 8, with  $r_S = 2.13$  ( $N_e = 8$ ) in CASP6.0. No experimental data available.

contribution of the bound electrons is evident for impact energies as low as 8 keV. Our total stopping describes the data from Refs. [13,46] (except for the value at 200 keV); however, they disagree with the experiments from Refs. [9,10] around the stopping maximum. As expected, SRIM [14] is semiempirical and fits the data around the maximum. Instead, the DPASS curve [45] is very close to ours, with the stopping maximum shifted to lower energies. We will comment on these data later in this paper when we present a scaling law valid for all the lanthanide experimental data.

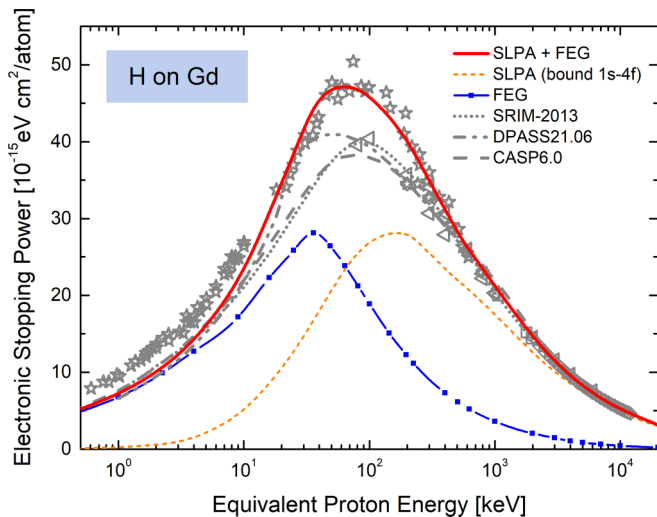


FIG. 14. Stopping cross section of Gd for H. Solid curves: present results using SLPA-LM—total (red solid line), bound electrons ( $1s-4f$ ) (orange short-dashed line), and FEG with  $r_S = 2.61$  ( $N_e = 3$ ) (blue squares-line). Discontinued curves: same as in Fig. 8, with  $r_S = 1.88$  ( $N_e = 8$ ) in CASP6.0. Symbols: experimental data from  $\diamond$  [46],  $\triangleleft$  [13],  $\square$  [48],  $\diamond$  [49], and recent measurements from  $\star$  [12].

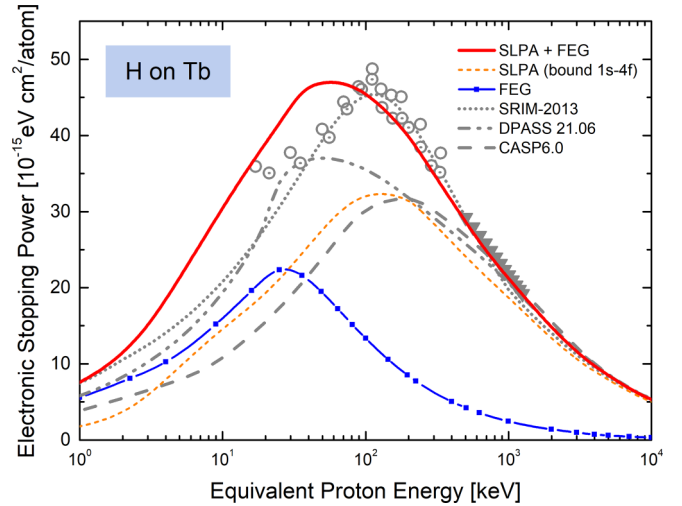


FIG. 15. Stopping cross section of Tb for H. Solid curves: present results using SLPA-LM—total (red solid line), bound electrons ( $1s-4f$ ) (orange short-dashed line), and FEG with  $r_S = 2.96$  ( $N_e = 2$ ) (blue squares-line). Discontinued curves: same as in Fig. 8, with  $r_S = 2.94$  ( $N_e = 2$ ) in CASP6.0. Symbols: experimental data from  $\circ$  [9],  $\odot$  [10], and equivalent values of He on Tb  $\blacktriangledown$  [50].

## 2. Cerium

Cerium is the first REE with  $4f$  electrons. However, as discussed in Sec. IV B, we considered it part of the FEG ( $N_e = 4$ ) and the rest of the electrons ( $1s-5p$ ) as bound. We display our electronic stopping cross sections in Fig. 8. The separation between the FEG and the total stopping curves evidences the bound electron contribution for impact energies above 5 keV. Our results agree well with the high-energy experiments by Knudsen *et al.* [46]. The values by Ref. [47] are lower than the expected high-energy limit of the stopping power. Further

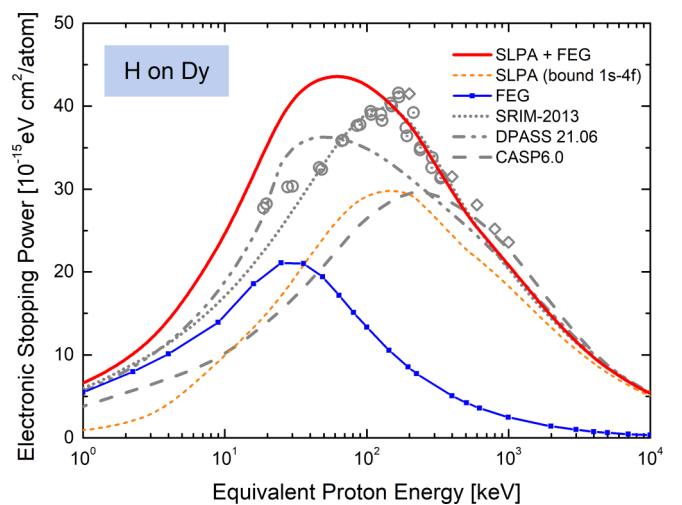


FIG. 16. Stopping cross section of Dy for H. Solid curves: present results using SLPA-LM—total (red solid line), bound electrons ( $1s-4f$ ) (orange short-dashed line), and FEG with  $r_S = 2.94$  ( $N_e = 2$ ) (blue squares-line). Discontinued curves: same as in Fig. 8, with  $r_S = 2.94$  ( $N_e = 2$ ) in CASP6.0. Symbols: experimental data from  $\diamond$  [46],  $\circ$  [9] and  $\odot$  [10].

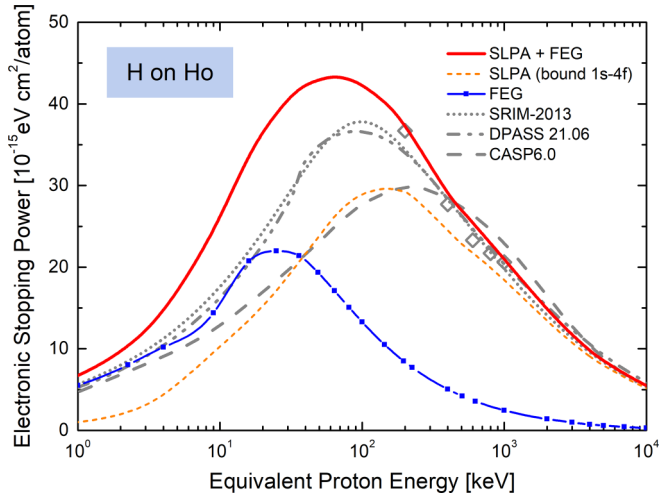


FIG. 17. Stopping cross section of Ho for H. Solid curves: present results using SLPA-LM—total (red solid line), bound electrons ( $1s-4f$ ) (orange short-dashed line), and FEG with  $r_S = 2.93$  ( $N_e = 2$ ) (blue squares-line). Discontinued curves: same as in Fig. 8, with  $r_S = 2.56$  ( $N_e = 3$ ) in CASP6.0. Symbols: experimental data from  $\diamond$  [46].

comments on this dataset [47] will be presented later in relation to the scaling. All the theoretical curves for energies above 400 keV agree quite well with the experimental values from Ref. [46]. For lower energies, our curve is closer to SRIM than to DPASS and CASP. However, the lack of data in this energy range makes our results nonconclusive.

### 3. Praseodymium

In Fig. 9, the stopping results for protons in Pr are displayed. In this case, the bound electrons contribute

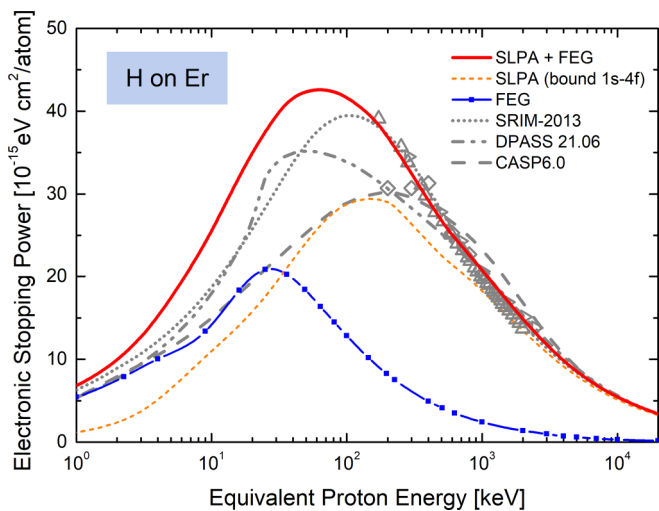


FIG. 18. Stopping cross section of Er for H. Solid curves: present results using SLPA-LM—total (red solid line), bound electrons ( $1s-4f$ ) (orange short-dashed line), and FEG with  $r_S = 2.91$  ( $N_e = 2$ ) (blue squares-line). Discontinued curves: same as in Fig. 8, with  $r_S = 2.31$  ( $N_e = 4$ ) in CASP6.0. Symbols: experimental data from  $\diamond$  [46],  $\triangle$  [51], and  $\triangleright$  [52].

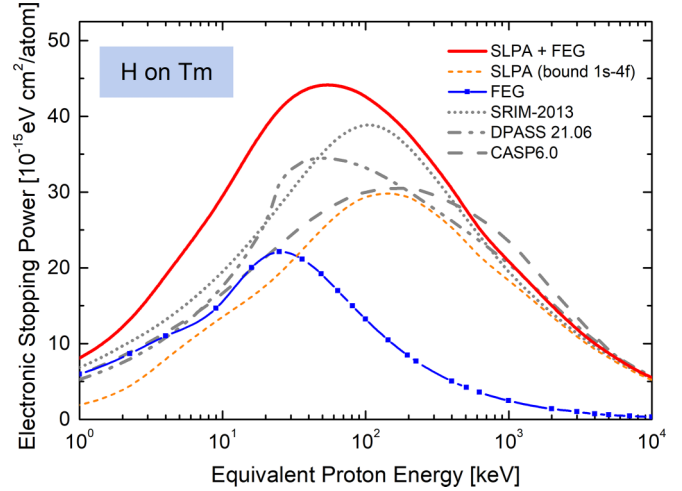


FIG. 19. Stopping cross section of Tm for H. Solid curves: present results using SLPA-LM—total (red solid line), bound electrons ( $1s-4f$ ) (orange short-dashed line), and FEG with  $r_S = 2.89$  ( $N_e = 2$ ) (blue squares-line). Discontinued curves: same as in Fig. 8, with  $r_S = 2.13$  ( $N_e = 5$ ) in CASP6.0. No experimental data available.

significantly to the total stopping power, even at impact energies as low as 1 keV. The small ionization gap of the  $4f$  electrons (2.6 eV) is mainly responsible for this feature. To emphasize our point, we illustrate in Fig. 9 the contribution of the  $4f$  electrons with an orange dash-dotted curve. We recall that the bound electron contribution was obtained with the SLPA-LM, which is a perturbative model, so values below 20 keV may underestimate the bound electron stopping power. The present results agree with the only set of experimental values by Knudsen *et al.* [46] in the high-energy range. The discrepancy among our results, SRIM, CASP, and DPASS, show

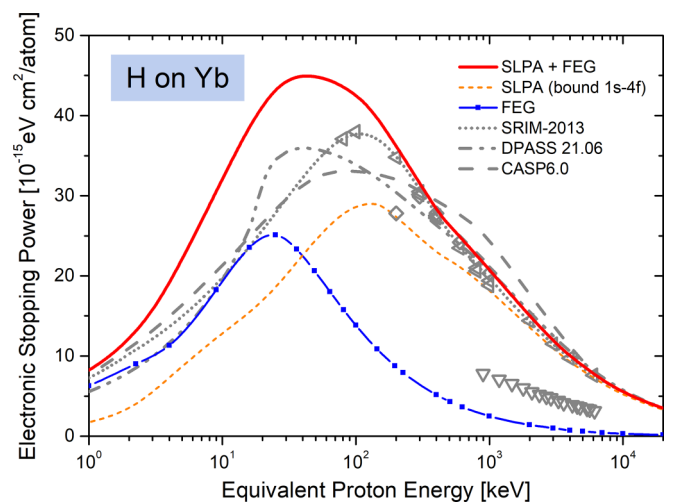


FIG. 20. Stopping cross section of Yb for H. Solid curves: present results using SLPA-LM—total (red solid line), bound electrons ( $1s-4f$ ) (orange short-dashed line), and FEG with  $r_S = 3.22$  ( $N_e = 2$ ) (blue squares-line). Discontinued curves: same as in Fig. 8, with  $r_S = 2.23$  ( $N_e = 6$ ) in CASP6.0. Symbols: experimental data from  $\diamond$  [46],  $\triangleleft$  [13], and  $\nabla$  [47].

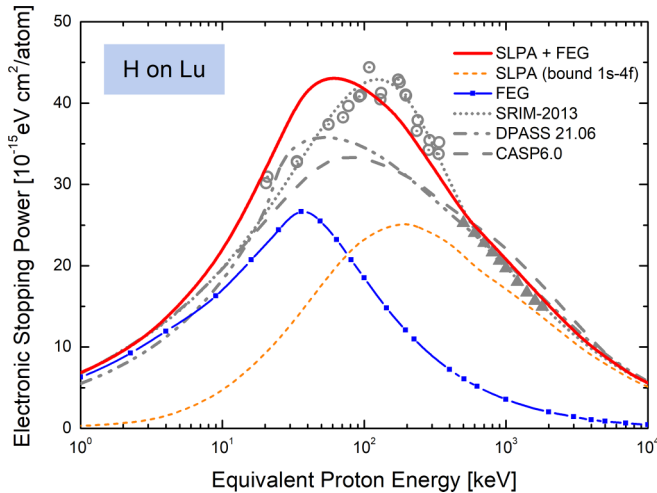


FIG. 21. Stopping cross section of Lu for H. Solid curves: present results using SLPA-LM—total (red solid line), bound electrons ( $1s-4f$ ) (orange short-dashed line), and FEG with  $r_s = 2.51$  ( $N_e = 3$ ) (blue squares-line). Discontinued curves: same as in Fig. 8, with  $r_s = 1.89$  ( $N_e = 7$ ) in CASP6.0. Symbols:  $\circ$  [9],  $\odot$  [10], and equivalent values of He on Lu  $\blacktriangle$  [53].

the need for new experimental data, mainly for energies  $E < 200$  keV.

#### 4. Neodymium

The stopping power for Nd is shown in Fig. 10. As in the case of Pr, bound electrons contribute significantly to the total stopping power at very low impact energies due to the small  $4f$  binding energy. Our results overestimate the data from Refs. [9,10]. As mentioned in Sec. I, these measurements have been proven to disagree with most of the experimental values for protons in other targets. The theoretical curves corresponding to DPASS and CASP do not describe the experimental values either.

#### 5. Promethium

Figure 11 displays the present theoretical stopping results for protons in Pm. The binding energy of the  $4f$  electrons is 8.8 eV, which is larger than for Pr and Nd. This feature shifts the threshold of the bound electron stopping power (orange short-dashed curve) to higher impact energies. Because of the radioactive nature of Pm, there are no experimental data to compare with. This lack of data could be solved by resorting to scaling laws valid for all elements, as will be mentioned later.

#### 6. Samarium

The results obtained for Sm are shown in Fig. 12. Remarkably, the present total stopping cross section agrees excellently with the experimental data [13] in the whole energy range. As seen in the figure, all the theoretical models (including SRIM) agree for energies below 10 keV and above 400 keV.

#### 7. Europium

In Fig. 13, we represent the total stopping corresponding to Eu. As in the case of Pr, no experimental data are available. The present results are generally in good agreement with the models analyzed thus far. We can note the difference with CASP at low energies. This overestimation is related to the number of electrons considered in the FEG. As presented in the previous section, we use  $N_e = 3$  while CASP considers  $N_e = 8$ .

#### 8. Gadolinium

The total stopping of Gd is presented in Fig. 14. Since there are enough experimental data to cover the entire energy range, we consider this element a benchmark for our model. These measurements can be separated into two groups, the data previous to 1990 [13,46,48,49] and the recent ones [12] (from 2017). Our results agree very well with the later ones for energies greater than 10 keV. Around the stopping maximum, the data by Sirotinin *et al.* [13] differ from these recent values. Correspondingly, SRIM fits its prediction to the data group published before 1990. Below 10 keV, all the theoretical models underestimate the experimental data by Roth *et al.* [12]. On a side note, the SPCC can describe these low-energy values if  $r_s = 1.75$  ( $N_e = 10$ , i.e., the electrons  $4f^7 5d 6s^2$  in the FEG) as suggested in Ref. [29]. However, this value for  $N_e$  is inconsistent with the current paper. Moreover, our total stopping power with  $N_e = 10$  and  $5p-1s$  bound describes the low-energy data but overestimates the rest.

#### 9. Terbium

We show the results obtained for Tb in Fig. 15. As in the case of Nd, the ionization gap of the  $4f$  electrons is very small. This feature accounts for the large bound electron contribution to the total stopping power at low energies. There are two sets of data [9,10], which describe the stopping maximum. Because no experimental data are available at high energies, we include recent measurements for He impact from Ref. [50] considering the  $Z_p^2$  dependence. These data are represented with filled symbols instead of hollow ones to remark they are not for proton impact. Our total stopping power cross sections agree with the experimental data above 90 keV. The present stopping maximum is located at  $E \simeq 50$  keV, which agrees with DPASS; however, the DPASS and CASP curves are much lower.

#### 10. Dysprosium

The results for Dy are shown in Fig. 16. The present stopping power agrees with the experimental values and SRIM only for impact energies above 150 keV. The theoretical-experimental comparison is very similar to Fig. 15 for Tb, with the advantage that, in this case, there are high-energy data available [46]. Our total stopping curve disagrees with the other theoretical models in the medium- and low-energy range.

### 11. Holmium

In Fig. 17, we include the present results for protons in Ho. Two comments can be raised: first, we describe all the experimental values from Ref. [46], even at 200 keV. Secondly, our results are larger than the other theoretical models around the stopping maximum and below. Evidently, measurements in the low-energy range for this target are required to solve the discrepancy of the stopping predictions in this region.

### 12. Erbium

The results obtained for Er are shown in Fig. 18. Our total stopping power agrees excellently with the experimental data in a wide range of energies, from 200 to 2500 keV. The medium- and low-energy regions are experimentally unexplored; measurements would be necessary to improve the knowledge of the stopping in this lanthanide.

### 13. Thulium

The total stopping of Tm for protons is displayed in Fig. 19. Together with Pm and Eu, this target is experimentally uninvestigated in the whole energy range. All the theoretical curves are very different, highlighting the unpredictability of the energy loss of protons in Tm. As mentioned before, a scaling law for the experimental data of joining experiments for all lanthanides could resolve this lack of data.

### 14. Ytterbium

Figure 20 shows the stopping power cross section for protons on Yb. Our calculations agree with measurements from Refs. [13] and [46] for energies above 200 and 300 keV, respectively. However, our values are higher than the other theoretical models in the intermediate- and low-energy regions. As in the case of Ce, the data by Ref. [47] are clearly outliers.

### 15. Lutetium

Finally, we present the stopping power of Lu in Fig. 21. The  $4f$  subshell is filled for this element, and the  $4f$  electrons are more tightly bound ( $E_{4f} = 10.6$  eV). Hence, the contribution of these electrons to the energy loss is shifted to higher energies. The comparison of our results with the experimental data around the curve maximum is rather good but shifted to lower energies. These data correspond to the Refs. [9,10] already mentioned. Since no experimental data are available for Lu in the high-energy range, we include recent He impact stopping power from Ref. [53] with the corresponding equivelocity conversion and normalized with  $Z_p^2$ . These data are represented with filled symbols.

The theoretical research carried out for the 15 solid lanthanides, the lack of data, and the doubts about many old measurements can be analyzed together, resorting to scaling laws. We consider the Lindhard scaling [54] of the dimensionless stopping number  $L = S v^2 / (4\pi Z_T)$  as a function of  $v^2/Z_T$ . These results are presented in Fig. 22. The validity of the scaling is impressive; all the present curves for 15 targets almost join in a single band. Moreover, all the experimental

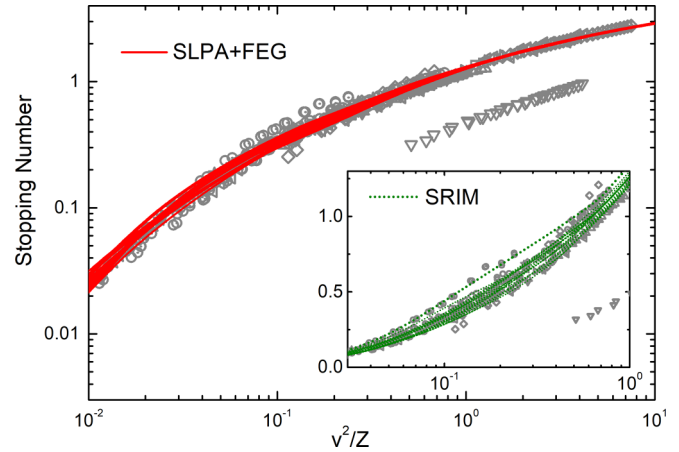


FIG. 22. Scaling of the stopping number  $L = S v^2 / (4\pi Z_T)$  for all the lanthanides. Solid curves: present results for total stopping number (SLPA+FEG). Symbols: experimental data, notation as in Figs. 7–21. Inset: the stopping number scaling for SRIM results.

data, together, cover almost the entire energy range. This is very interesting and useful because it could be employed to predict values for new measurements. The scaling also makes outliers more evident. The data for Ce and Yb ( $\nabla$  [47]) lay remarkably outside the general tendency. Also, the data measured by Refs. [9,10] ( $\circ$  and  $\odot$ ) do not fully follow the scaling, in particular for lanthanum at intermediate energies. To further analyze these discrepancies, we performed a similar plot for the SRIM results, which is displayed in the inset. The semiempirical nature of this approach leads SRIM to wrongly follow these questioned experimental values.

## V. CONCLUSIONS

We present in this paper a systematic study of the stopping power of protons in the 15 lanthanides: from La (57) to Lu (71). We aim to resolve certain open issues related to the  $4f$  subshell. We compute the electronic structure of the atomic targets (gaseous state). Understandably, we find discrepancies for the valence and subvalence shells when comparing our results with binding energies measured in solid lanthanides. We analyze the valence shell as the conduction band of metallic lanthanides. Based on the systematic study of the atomic structure and the available literature, we consider the FEG composed of the  $6s^2$  electrons plus the  $5d$  (if there are any). For the light lanthanides (Ce to Eu), one  $4f$  electron is promoted to the conduction band, while none for the heavy lanthanides (Gd to Lu). The number of electrons proposed in the FEG agrees, in some cases, with experimentally inferred values and, in others, with theoretically derived ones.

The stopping power results are obtained from a combination of bound and valence electron contributions to the energy loss. The electronic stopping of inner shells is modeled with the SLPA-LM approach. In contrast, for the FEG, we use the SPCC model for energies below the plasmon excitation energy and the Mermin-Lindhard dielectric formalism above this value.

In general, the stopping experimental measurements for REEs are quite old (previous to 1990). Moreover, there are only ten sources of data published for the 15 lanthanides, and

they only cover the high-energy region except for Gd. Our results describe rather well the experimental stopping cross sections, except for the low-energy values in Gd and some data sets around the maximum. Particularly, for La, Nd, and Dy, the only data around the maximum are the ones included in Refs. [9,10]. We draw attention to this publication since measurements for well-known targets (Al, Au, Ag, Ta, and Pt) have shown inconsistencies with many other values available in the literature. It is worth mentioning that the semiempirical SRIM describes these data as they are the only ones in some of the lanthanides.

Even though most uses of lanthanide data involve alloys and oxides, the energy loss in compounds is predominantly approximated by adding individual atomic stopping powers.

Throughout this paper, we have shown that the predictive capability of the atomic stopping in REEs is nonconclusive due to the lack of experimental measurements, mainly in the intermediate- (stopping maximum) and low-energy regions. We stress the necessity of new experimental efforts sustained by the importance of lanthanides.

#### ACKNOWLEDGMENTS

The following institutions of Argentina financially support this research: the CONICET by Project No. PIP11220200102421CO, the ANPCyT by Project No. PICT-2020-SERIE A-01931, and the University of Buenos Aires by Project No. 20020170100727BA.

- 
- [1] A. S. Patil, A. V. Patil, C. G. Dighavkar, V. A. Adole, and U. J. Tupe, *Chem. Phys. Lett.* **796**, 139555 (2022).
- [2] R. Friedman, *J. Phys. Chem. B* **125**, 2251 (2021).
- [3] A. Pedrielli, P. de Vera, P. E. Trevisanutto, N. M. Pugno, R. Garcia-Molina, I. Abril, S. Taioli, and M. Dapor, *Phys. Chem. Chem. Phys.* **23**, 19173 (2021).
- [4] C. Kratochwil, F. L. Giesel, M. Eder, A. Afshar-Oromieh, M. Benešová, W. Mier, K. Kopka, and U. Haberkorn, *Eur. J. Nucl. Med. Mol. Imaging* **42**, 987 (2015).
- [5] C. C. Montanari, P. A. Miranda, E. Alves, A. M. P. Mendez, D. M. Mitnik, J. E. Miraglia, R. Correa, J. Wachter, M. Aguilera, N. Catarino, and R. C. da Silva, *Phys. Rev. A* **101**, 062701 (2020).
- [6] J. P. Peralta, M. Fiori, A. M. P. Mendez, and C. C. Montanari, *Phys. Rev. A* **105**, 062814 (2022).
- [7] C. C. Montanari, C. D. Archubi, D. M. Mitnik, and J. E. Miraglia, *Phys. Rev. A* **79**, 032903 (2009).
- [8] C. C. Montanari, D. M. Mitnik, C. D. Archubi, and J. E. Miraglia, *Phys. Rev. A* **80**, 012901 (2009).
- [9] T. Krist and P. Mertens, *Nucl. Instrum. Methods Phys. Res., Sect. B* **218**, 790 (1983).
- [10] T. Krist and P. Mertens, *Nucl. Instrum. Methods Phys. Res., Sect. B* **218**, 821 (1983).
- [11] C. C. Montanari and P. Dimitriou, *Nucl. Instrum. Methods Phys. Res., Sect. B* **408**, 50 (2017); H. Paul and C. C. Montanari, Electronic Stopping Power of Matter for Ions Graphs, Data, Comments and Programs, <https://www-nds.iaea.org/stopping/>.
- [12] D. Roth, B. Bruckner, M. V. Moro, S. Gruber, D. Goebel, J. I. Juaristi, M. Alducin, R. Steinberger, J. Duchoslav, D. Primetzhofer, and P. Bauer, *Phys. Rev. Lett.* **118**, 103401 (2017).
- [13] E. I. Sirotinin, A. F. Tulinov, V. A. Khodyrev, and V. N. Mizgulin, *Nucl. Instrum. Methods Phys. Res., Sect. B* **4**, 337 (1984).
- [14] J. F. Ziegler, computer code SRIM, 2013, <http://www.srim.org/>.
- [15] E. Kennedy, C. Choi, and M. C. Scott, [arXiv:2101.06794](https://arxiv.org/abs/2101.06794).
- [16] C. C. Montanari and J. E. Miraglia, in *Advances in Quantum Chemistry: Theory of Heavy Ion Collision Physics in Hadron Therapy*, edited by D. Belkic (Elsevier, New York, 2013), Vol. 2, Chap. 7, pp. 165–201.
- [17] C. C. Montanari and J. E. Miraglia, *Phys. Rev. A* **96**, 012707 (2017).
- [18] A. Bar-Shalom, M. Klapisch, and J. Oreg, *J. Quant. Spectrosc. Radiat. Transfer* **71**, 169 (2001).
- [19] I. Grant, *Adv. Phys.* **19**, 747 (1970).
- [20] J. Lindhard and M. Scharff, K. Dan. Vidensk. Selsk. Mat.-Fys. Medd. **27**, 1 (1953).
- [21] P. M. Echenique, F. Flores, and R. H. Ritchie, *Dynamic Screening of Ions in Condensed Matter* (Academic, New York, 1990), pp. 229–308.
- [22] P. Sigmund, *Particle Penetration and Radiation Effects, General Aspects and Stopping of Swift Point Charges* (Springer-Verlag, Berlin, 2006), Vol. 1.
- [23] C. C. Montanari and J. E. Miraglia, *Nucl. Instrum. Methods Phys. Res., Sect. B* **460**, 27 (2019).
- [24] N. D. Mermin, *Phys. Rev. B* **1**, 2362 (1970).
- [25] C. C. Montanari and J. E. Miraglia, *AIP Conf. Proc.* **1525**, 259 (2013).
- [26] C. C. Montanari, D. M. Mitnik, and J. E. Miraglia, *Radiat. Eff. Defects Solids* **166**, 338 (2011).
- [27] M. Oswal, S. Kumar, U. Singh, S. Singh, G. Singh, K. P. Singh, D. Mehta, A. M. P. Mendez, D. M. Mitnik, C. C. Montanari, D. Mitra, and T. Nandi, *Radiat. Phys. Chem.* **176**, 108809 (2020).
- [28] J. E. Miraglia and M. S. Gravielle, *Phys. Rev. A* **78**, 052705 (2008).
- [29] A. M. P. Mendez, C. C. Montanari, and D. M. Mitnik, *Nucl. Instrum. Methods Phys. Res., Sect. B* **460**, 114 (2019).
- [30] G. P. Williams, *Electron Binding Energies of the Elements*, 95th ed. (CRC, Boca Raton, FL, 2014), Chap. 10, pp. 200–205.
- [31] J. A. Bearden and A. F. Burr, *Rev. Mod. Phys.* **39**, 125 (1967).
- [32] S. Cotton, Electronic and magnetic properties of the lanthanides, in *Lanthanide and Actinide Chemistry* (Wiley, New York, 2006), Chap. 5, pp. 61–87.
- [33] K. O. Kvashnina, S. M. Butorin, and P. Glatzel, *J. Anal. At. Spectrom.* **26**, 1265 (2011).
- [34] E. Puppini, I. Lindau, and I. Abbati, *Solid State Commun.* **77**, 983 (1991).
- [35] C. Colliex, M. Gasgnier, and P. Trebbia, *J. Phys. France* **37**, 397 (1976).
- [36] B. Johansson and S. Li, *Philos. Mag.* **89**, 1793 (2009).
- [37] A. G. Nargizyan and Yu. A. Uspenskii, *J. Exp. Theor. Phys.* **76**, 530 (1993).

- [38] L. Ward, in *Handbook of Optical Constants of Solids*, edited by E. D. Palik (Academic, New York, 1997), pp. 287–340.
- [39] C. C. Montanari, J. E. Miraglia, and N. R. Arista, *Phys. Rev. A* **62**, 052902 (2000).
- [40] T. L. Ferrell and R. H. Ritchie, *Phys. Rev. B* **16**, 115 (1977).
- [41] M. D. Z. Ziegler and J. P. Biersack, computer code SRIM, 2008.
- [42] P. L. Grande and G. Schiwietz, computer code CASP, version 6.0, 2021, <http://www.casp-program.org/>.
- [43] F. Matias, R. C. Fadanelli, P. L. Grande, N. R. Arista, N. E. Koval, and G. Schiwietz, *Phys. Rev. A* **98**, 062716 (2018).
- [44] A. Schinner and P. Sigmund, *Nucl. Instrum. Methods Phys. Res., Sect. B* **460**, 19 (2019).
- [45] A. Schinner and P. Sigmund, computer code DPASS21.06, 2020, <https://www.sdu.dk/en/dpass>.
- [46] H. Knudsen, H. Andersen, and V. Martini, *Nucl. Instrum. Methods Phys. Res. Sect. B* **168**, 41 (1980).
- [47] E. I. Sirotnin, A. F. Tulinov, A. Fiderkevich, and K. S. Shyshkin, *Radiat. Eff.* **15**, 149 (1972).
- [48] K. Ogino, T. Kiyosawa, and T. Kiuchi, *Nucl. Instrum. Methods Phys. Res., Sect. B* **33**, 155 (1988).
- [49] H. H. Andersen, H. Simonsen, H. Sørensen, and P. Vajda, *Phys. Rev.* **186**, 372 (1969).
- [50] S. Kumar and P. K. Diwan, *Radiat. Eff. Defects Solids* **173**, 970 (2018).
- [51] J. C. Oberlin, A. Amokrane, H. Beaumevieille, J. P. Stoquert, and R. P. de la Bathie, *J. Phys. France* **43**, 485 (1982).
- [52] R. A. Langley and R. S. Blewer, *Nucl. Instrum. Methods Phys. Res., Sect. B* **132**, 109 (1976).
- [53] W. H. Trzaska, G. N. Knyazheva, J. Perkowski, J. Andrzejewski, S. V. Khlebnikov, E. M. Kozulin, T. Malkiewicz, M. Mutterer, and E. O. Savelieva, *Nucl. Instrum. Methods Phys. Res., Sect. B* **418**, 1 (2018).
- [54] J. Lindhard and M. Scharff, *Phys. Rev.* **85**, 1058 (1952).